Universitat Politècnica de Catalunya (UPC)
Universitat Autònoma de Barcelona (UAB)
Universitat de Barcelona (UB)
Institut de Ciències Fotòniques (ICFO)

http://www.photonicsbcn.eu

Master in Photonics

MASTER THESIS WORK

COHERENT CONTROL OF A SUPERCONDUCTING QUANTUM BIT

Rafael Luque Merino

Supervised by Dr. Pol Forn Díaz, (BSC/IFAE), co-supervised by Prof. Jordi Mompart Penina (UAB)

Presented on date 6th September 2019

Registered at

Escola Tècnica Superior d'Enginyeria de Telecomunicació de Barcelona

Coherent control of a superconducting quantum bit

Rafael Luque Merino

Institut Català de Nanociència i Nanotecnologia (ICN2)
Campus UAB, 08193 Bellaterra (Barcelona)

E-mail: rluque01@ucm.es

September 2019

Abstract. Transmon qubits are at the forefront of solid state platforms for quantum computing. In this thesis, results obtained from the experimental study of a transmon qubit in a 3D cavity are presented. A complete view of the experiment is given, including cryogenic methods, microwave signal processing and spectroscopic and pulsed measurements of the transmon qubit. Lastly, partial results on state discrimination set the next step towards fully coherent control of the qubit.

1. Introduction

Over the last three decades, Quantum Information Processing (QIP) has seen major advancements both in theory and experiment. Within the current landscape, quantum computing holds strong promise of harnessing the unique properties of quantum systems in order to compute and solve very hard problems for classical computers [1]. The basic unit of information in any quantum computing system is the qubit or quantum bit. Superconducting circuits are one of the leading qubit platforms, as they have high coherence, they are scalable and their parameters can be tuned during fabrication[2]. Other qubits, such as electron spins or ions, are not tunable at all. The transmon qubit [3] is a superconducting circuit based on a Josephson junction, with transition energies in the microwave regime.

The main challenge of conducting an experiment with qubits is the interplay between isolation from the environment (ultra high vacuum, cryogenic temperature) and accurate interaction with the setup. Fast and accurate signals are required to manipulate the state of the qubit and read out its state, while remaining highly isolated from the 'outside' to avoid decoherence. In this thesis, we will work with a transmon qubit, which is located inside a 3D aluminum cavity for electromagnetic (EM) fields. Transmon qubits in 3D cavities have yielded some of the best coherence times across all qubit platforms, with coherence times up to 100 microseconds [4]. Over the next chapters we will introduce the key concepts, detail the experimental setup and present measurements of the coherent control of a transmon qubit inside a 3D cavity.

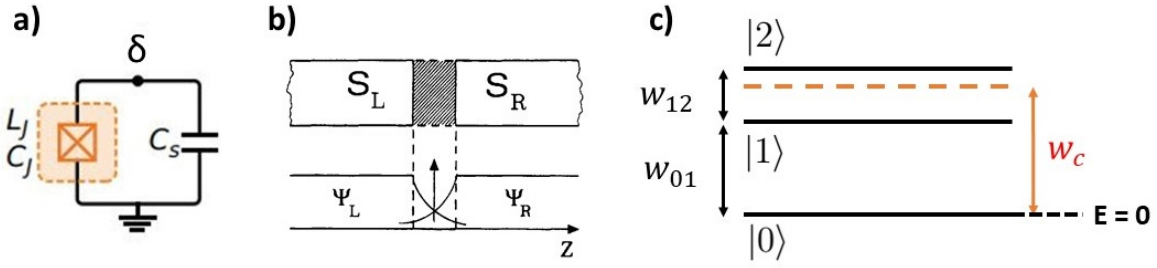

Figure 1: a) Equivalent circuit of the transmon qubit, where δ denotes the phase difference across the JJ; C_J, L_J are the junction's capacitance and inductance, and C_S is the shunting capacitance. b) Schematic view of the JJ, with the superconducting wavefunctions Ψ_L and Ψ_R overlapping over the oxide barrier. c) Energy diagram of the qubit-cavity system, showing the transmon's anharmonicity.

2. Methods

2.1. Transmon qubit 101

The transmon qubit is a superconducting circuit based on a Josephson Junction (JJ) shunted by a big capacitance in parallel. The JJ is the key element of the transmon qubit, consisting of a weak insulating barrier between two superconducting electrodes. The device is fabricated through the deposition of a thin film of aluminum on a silicon substrate, in addition to selective oxidation of the aluminum in the JJ. The transmon qubit can be modelled as an LC circuit whose Hamiltonian has the energy spectrum of a harmonic oscillator. The two distinct superconductor wavefunctions $\Psi_L = |\Psi_L|e^{i\delta_L}$, $\Psi_R = |\Psi_R|e^{i\delta_R}$ at each side of the junction (Figure 1b) can interact through the aluminum oxide layer. The overlap of the two distinct wavefunctions allows tunneling of Cooper pairs [5]. Transport through the JJ is governed by the Josephson relations:

$$I = I_c \, sin(\delta) \quad , \quad V = \frac{\Phi_0}{2\pi}\frac{d\delta}{dt} \tag{1}$$

where $\delta = \delta_1 - \delta_2$ is the phase difference across the junction, I_c is the critical current of the junction and $\Phi_0 = \frac{h}{2e}$ is a flux quantum. These relations characterize the JJ as a nonlinear inductor, turning the LC circuit into an anharmonic oscillator in which we can address each transition separately thanks to their different energy level transitions. Sketches of the transmon's equivalent circuit and the JJ are shown in Figure 1a and 1b.

The JJ is also characterized by its Josephson energy $E_J = \frac{\Phi_0 I_c}{2\pi}$. Transmon qubits feature a large shunting capacitance C that leads to a small charging energy $E_C = \frac{e^2}{2C_T}$ (where $C_T \approx C$ is the total capacitance). A large ratio $E_J/E_C \gg 1$ characterizes the transmon regime, in which the transmon qubit is not sensitive to charge noise. The qubit Hamiltonian can be quantized using the charge $\hat{Q}$ (number of Cooper pairs) and phase difference across the junction ($\hat{\delta}$) as canonical variables [6]. We will drop the hats from operators from this point forward.

The Hamiltonian reads as:

$$H = \frac{Q^2}{2C} + E_J[1 - cos(\delta)] \tag{2}$$

It describes the transmon qubit as an anharmonic oscillator due to the presence of the JJ. The anharmonicity α=$w_{12} - w01$ is crucial as it provides us with unique transitions that we can address with adequate microwave pulses (Figure 1c).

2.2. Dispersive readout

The transmon is located inside a rectangular aluminum cavity . The dimensions of the cavity are chosen so that the TE101 mode is in the microwave regime (1-10 GHz), with other modes far enough from this mode. In particular, our cavity has a resonant mode at $\frac{w_c}{2\pi} = 7.890$ GHz. The transmon chip is located in the center of the cavity, parallel to the field lines of the TE101 mode, so that the qubit-field coupling g is maximal. The interaction between the qubit and the cavity (resonator) can be described using the Jaynes - Cummings Hamiltonian [7, 8]:

$$H_{JC} = \hbar[w_c(a^\dagger a + 1/2) + \frac{w_q}{2}\sigma_z + g(\sigma_+ a + \sigma_- a^\dagger)] \tag{3}$$

If there is a large detuning between the cavity and qubit modes $|\Delta| = |w_q - w_r| \gg g$, there will not be an effective exchange of energy between qubit and cavity. This is known as the 'dispersive' limit, in which the Jaynes - Cummings Hamiltonian can be approximately diagonalized to take this form:

$$H_{disp} = \hbar[(w_c + \chi\sigma_z)(a^\dagger a + 1/2) + \frac{\widetilde{w_q}}{2}\sigma_z] \tag{4}$$

where $\chi = \frac{g^2}{\Delta}$ is the shift on the dressed cavity modes, Δ is the detuning, g represents the coupling strength and $\widetilde{w_q} = w_q + \frac{g^2}{\Delta}$ is the Lamb-shifted qubit frequency [10]. In the dispersive limit, the presence of the qubit results on a state-dependent shift of the cavity mode frequency by $\pm\chi$. In addition, the qubit frequency suffers a Lamb shift from the cavity vacuum. The exact frequency of the dressed cavity modes depends on the exact detuning Δ. In our system, the cavity mode has higher energy than the 0 - 1 transition of the qubit (see Figure 1c), resulting in the dressed cavity modes being above the bare cavity mode ($w_c^{|0\rangle}, w_c^{|1\rangle} \gg w_c$)

The qubit state-dependent shift of the cavity frequency $w_c = w_c(\langle\sigma_z\rangle)$ constitutes the principle for dispersive readout. Information about the state of the qubit can be inferred from the transmission through the dressed cavity modes. In the limit of few photons in the cavity, the dispersive Hamiltonian H_{disp} conmutes with σ_z ($[H_{disp}, \sigma_z] = 0$), allowing the dispersive readout to be a Quantum Non-Demolition measurement (QND) [10]. Importantly, there is a critical photon number $n_c = \frac{\Delta^2}{4g^2}$ for which the cavity becomes 'saturated', washing out the effect of the qubit. Then, there is a single cavity mode (the bare cavity mode) instead of having two dressed modes. This will be clear through our spectroscopic measurements in Section 3.2.

2.3. Cryogenic setup

As the superconducting gap of aluminum thin films is relatively high, around 300 μV, the limiting energy scale for our system is the energy separation between the qubit levels. A

transition frequency of ∼5 GHz corresponds to an effective temperature of ∼250 mK, which sets the operating temperature to be about 25 mK (a factor of 10 below the limiting energy scale, in order to minimize the thermal probability of qubit excitation) [9]. To achieve this temperature, a Leiden Cryogenics ^3He -^4He dry dilution refrigerator is used. It consists of 5 plates going from 50 K to 25 mK, physically shielded from the outside and controlled by a set of vacuum pumps. The aluminum cavitiy containing the qubit is located in the mixing chamber, which is cooled below 25 mK by the circulation of ^3He between two distinct phases of the ^3He -^4He mixture [11]. Embedded in the coaxial lines that reach the sample, there are several attenuators, filters and circulators to ensure protection of the equipment and reduction of electronic noise. In addition, there is a low-temperature high electron mobility transistor (HEMT) amplifier helps acquiring the signals. The system is monitored with a set of temperature and pressure gauges.

2.4. Electronic setup

The electronic setup starts with three radio frequency (RF) sources (NI QuickSyn FSW-0020, Rohde Schwarz SGS100A x2) which provide the local oscillator (LO) signals (200 MHz - 20 GHz). One of them is a vector source, meaning that it can be used to perform IQ modulation if fed with two intermediate frequency (IF) signals (10-100 MHz). This feature is very useful for the RF heterodyne detection method used to control and read out the qubit, detailed in Section 2.5. Marki Microwave IQ 4509 LXP mixers are used for upconversion and downconversion of the microwave pulses, while also providing IQ modulation capabilities. The IF waveforms are generated with a Keysight PXIe M3201a Arbitrary Waveform Generator (AWG), with a 1GS/s sample rate and a 400 MHz bandwidth. Using its 4 channels, up to two simultaneous waveforms can be generated, with independent control of the four total in-phase (I) and quadrature (Q) components of said waveforms. A Keysight PXIe M3102a Digitizer with 500 MS/s sample rate, 100 MHz bandwidth, with an on-board FPGA is used for signal acquisition, demodulation, and averaging of the pulses transmitted through the sample. A chain of room temperature

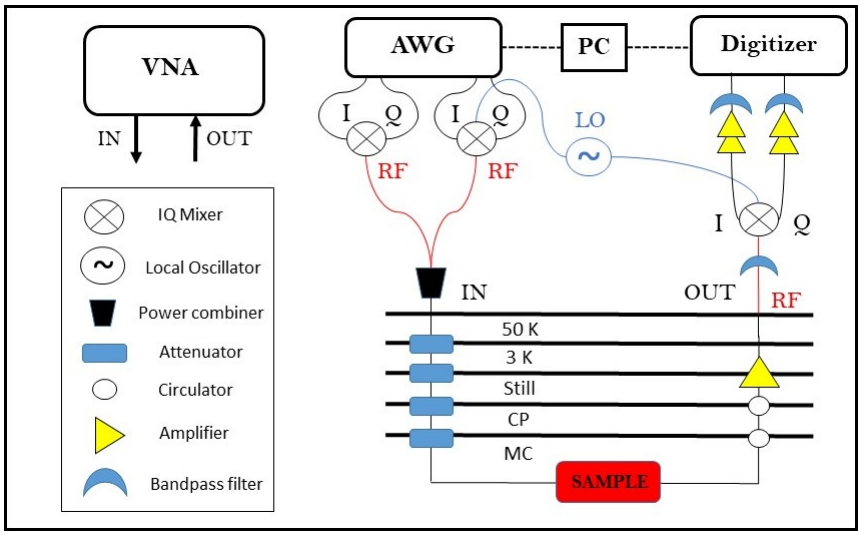

Figure 2: Schematic view of the cryogenic and electronic setup of the experiment

amplifiers is set before the digitizer to amplify the weak signals (usually reaching the sample at the one-photon power level). Several band-pass and low-pass filters (Mini-Circuits) are present in the setup, protecting the lines that go into the cryostat and filtering the acquired IQ traces. A Rubidium frequency standard is the origin of 10 MHz synchronization for all the devices. In addition, a Rohde Schwarz SPIE Test Receiver is used to analyze the spectrum of the generated signals and a high-frequency Vector Network Analyzer (VNA) Agilent PNA-X N5245A is used to perform spectroscopic measurements of the qubit and the cavity. Lastly, a Mini-Circuits ZFSC210G+ beam splitter is used to combine microwave signals at the input line of the cryostat, allowing to probe the cavity and qubit modes simultaneously. Most of the electronic devices are controlled using the software Labber. A schematic picture of the complete setup for coherent control is shown in Figure 2.

2.5. Heterodyne detection

In order to perform high fidelity readout of the state of the qubit, we employ radio frequency heterodyne detection in which the in-phase (I) and quadrature (Q) components of the readout pulse are acquired. From this complex representation of the signal, both the amplitude and the phase of the transmitted readout pulse can be determined. In the end, the goal is to digitize the real-time IQ components into a static ensemble average. The generated waveforms have independently tailored IQ components which allow the use of complex drivings of the qubit, such as adiabatic protocols [12, 13]. Importantly, it is not feasible to generate precise waveforms in the microwave regime with state of the art electronics. Instead, the waveforms will be generated at an intermediate frequency (our choice is 70 MHz). Using the IQ mixers and an RF source as local oscillator, these waveforms can be upconverted to the desired microwave frequency, while retaining the exact structure of the IQ waveforms.

The procedure for RF heterodyne detection is as follows. First, the exact IQ waveforms are generated at $w_{IF} = 70$ MHz, then upconverted into the GHz regime. The qubit drive and the readout pulses at the cavity modes will have different frequency. The pulses are sent into the cryostat through a set of filters and attenuators. The qubit drive pulses will reach the cavity at the power level of a single microwave photon ($\sim$ -135 dBm), while the readout pulses may have larger amplitude. After being transmitted through the cavity, the readout pulse is filtered and amplified before reaching the room temperature stage. There, another IQ mixer demodulates the signal using an exact copy of the previously used LO signal. At the outputs of the measurement chain, the time-dependent IQ components $I(t)$, $Q(t)$ are obtained. These signals, which oscillate at w_{IF}, are very weak so they are fed into a chain of room-temperature amplifiers. Bandpass filters around 70 MHz ensure that the amplifiers receive a clean signal, which is then directed onto our digitizer. The digitizer will acquire the IQ components separately over a specific time window, taking into account the ring-up time of the cavity. The digitizer, after demodulating at w_{IF}, yields the sampled IQ components which are then averaged over many measurements in order to estimate the final I and Q values. The amplitude and phase of the readout pulse can be computed from the IQ values as:

$$A = \sqrt{I^2 + Q^2} \quad , \quad \theta = arctan\ (Q/I) \tag{5}$$

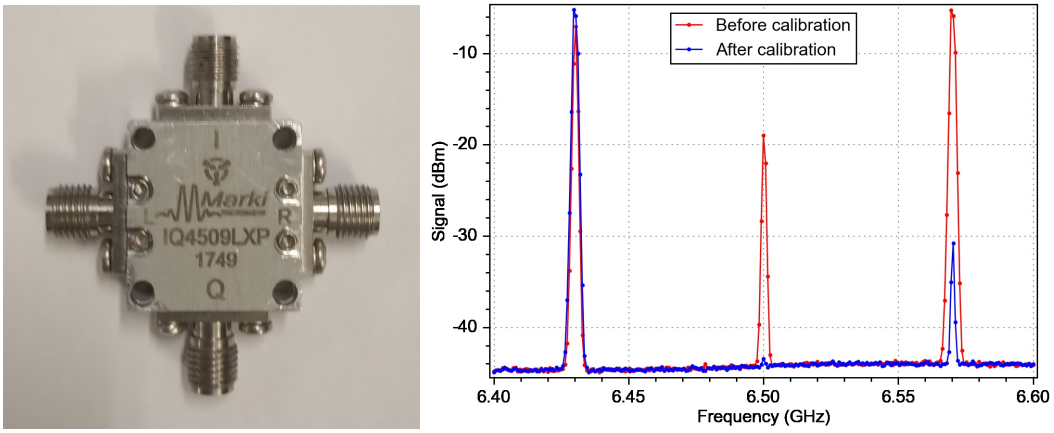

Figure 3: a) IQ mixer used for upconversion of the qubit drive pulses. b) Calibrated spectrum of the pictured IQ mixer, maximizing its lower sideband at 6.43 GHz.

3. Experimental results

3.1. IQ Mixer calibration

First, a calibration of the IQ mixers used for upconversion is presented. IQ mixers are 4-port microwave components that take as input an LO signal w_{LO} and two IF signals w_{IF} on the I and Q ports. At the output, the signals are multiplied giving raise to new frequencies w_{RF}:

$$w_{RF} = w_{LO} \pm n \cdot w_{IF} \tag{6}$$

where n = 0,1,2,3... represents the leakage of the LO signal (n=0) and the appearence of higher harmonics (n = 2,3...). It is crucial to generate microwave pulses that are resonant with the qubit transition or the cavity modes, without other spectral components disturbing this interaction. IQ mixer calibration is performed in two steps. First, the LO leakage is suppressed by adjusting the DC offsets on the I and Q ports of the mixer separately. Secondly, one sideband can be maximized over the other by adjusting the phase and amplitude of the I and Q waveforms. Figure 5 shows one of the used IQ mixers with its spectrum before and after calibration for the lower sideband at 6.43 GHz, using an LO signal of 6.5 GHz.

3.2. Spectroscopic measurements

We start by verifying the resonant frequency of the cavity, as well as the presence of the qubit. A punchout measurement of the cavity is performed using the high frequency VNA. In the punchout, the transmission is monitored while the frequency and power of the probe signal is varied. At low powers, we expect the cavity mode to have been shifted by the presence of the qubit $w_c = w_c(\langle\sigma_z\rangle)$, according to the dispersive readout limit. Nevertheless, it is necessary to probe at higher powers until we reach the critical photon number n_c for which the cavity would saturate to a single resonant mode, the bare cavity frequency. This will certify the presence of the qubit [5]. The punchout measurements are shown in Figure 4. The maximum in transmission (resonance with the cavity mode) shifts from the low power to the high power

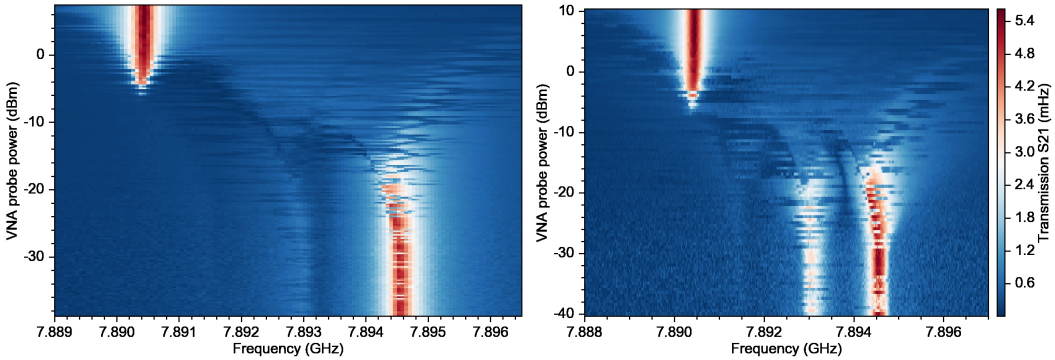

Figure 4: a) Punchout measurement of the cavity. The shifted resonance for low powers signals the presence of the qubit. b) Punchout with qubit excitation. Second cavity dressed mode appears more clearly. Both graphs share the same color bar, where red represents high transmission and blue represents low transmission

regime, signaling that the qubit is affecting the resonant mode of the cavity. In Figure 4a, a 'shadow' resonance seems to appear at low powers ($\sim$ 7.893 GHz). The system is absorbing radiation at this frequency with low probability, leading to its weak signature in the punchout measurement.

The punchout provides limited information about the qubit. To identify its lowest resonant frequency (0-1 transition) we perform two-tone spectroscopy. We set the probe tone in the VNA at the cavity dressed state ($\frac{w_c^{|0\rangle}}{2\pi}$ = 7.8945 GHz), where the transmission is maximum since the signal is on-resonance. Then, the second microwave tone is swept in a range around the estimated transition frequency of the qubit, which is given by the fabrication parameters and usually lies around 5 GHz. Once the second microwave tone is resonant with the qubit, the qubit is excited into its first excited level, changing the value of $\langle\sigma_z\rangle$ and consequently changing the resonant cavity mode frequency. Therefore, a dip in the transmission through the first dressed cavity mode $w_c^{|0\rangle}$ will signal the qubit transition frequency.. Figure 5 shows a two-tone spectroscopy measurement. The qubit 0-1 transition is identified at 4.81 GHz, while at higher powers another resonance appears at 4.66 GHz. This resonance corresponds to a 0-2 qubit transition enabled by a two-photon process, which occurs at a frequency $w_{02} = \frac{w_{01}+w_{12}}{2}$ as the transmon qubit is anharmonic. Further transitions can be identified, such as the 1-2 transition at 4.49 GHz which only appears at higher powers as it relies on the thermal population of the excited level of the qubit [9]. All resonances are also power-broadened. It is important to note that the VNA outputs continuous microwave signals, so the qubit is often in a mixed state between $|0\rangle$ and $|1\rangle$ when the measurement of the cavity is performed. For coherent control of the qubit, it is necessary to have precise timing between the drive and readout pulses. Having identified the main transition energies of the qubit, the punchout may be revisited by adding a second microwave tone that will excite the qubit. In this way the second dressed mode of the cavity $w_c^{|1\rangle}$ becomes more visible, as shown in Figure 4b. The 'shadow' resonance is now clearly identified, confirming the validity of the dispersive readout method. Experimentally obtained parameters are shown in Appendix A.

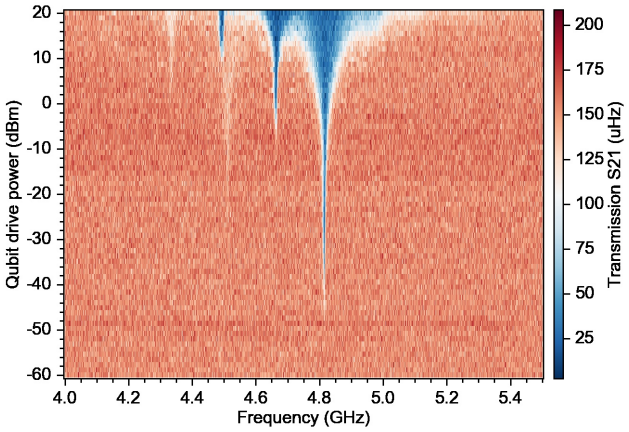

Figure 5: Two tone spectroscopy. The first three qubit transitions are visible. Red colors indicate high transmission, while blue represents low transmission.

3.3. Pulsed Measurements

To coherently manipulate the state of the qubit, it is not enough to identify its transition frequencies. Well-timed, fast and coherent microwave pulses must be used for qubit control and readout. The next step is performing pulsed measurements, in which the IQ waveforms are upconverted to the GHz regime in order to drive the qubit and extract information about its state. It is important to note that all resonances will appear 70 MHz above its value, due to the upconversion of the pulses (Equation 6). Firstly, the punchout measurement is reproduced with short microwave pulses. Figure 6a shows a few microseconds pulse being resonantly transmitted through the bare cavity mode w_c (high power). In Figure 6b, The magnitude of the pulses (after demodulation) is largest at the $w_c^{|0\rangle}$ mode, reproducing the spectroscopic measurements. Examples of the used waveforms are presented in Appendix B.

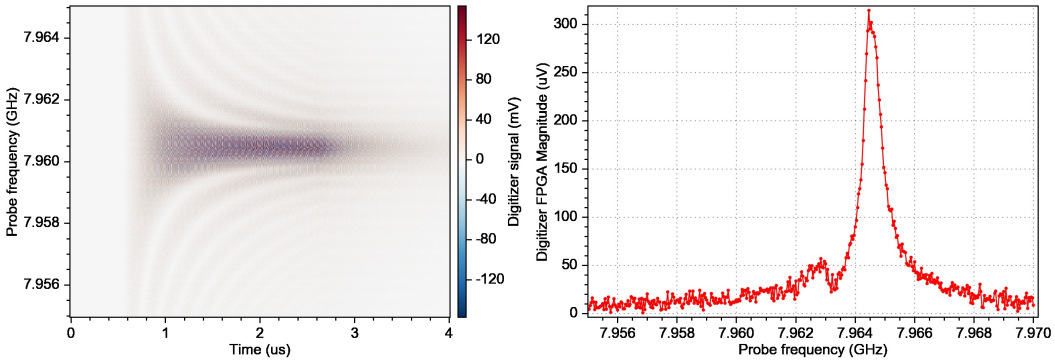

Figure 6: a) Bare cavity resonance at 7.89 GHz (+70MHz) measured with a short microwave pulse. b) Magnitude of the transmitted pulses over the cavity resonance. Both cavity dressed modes appear at 7.893 GHz ($w_c^{|1\rangle}$) and 7.8945 GHz ($w_c^{|0\rangle}$) (+70MHz)

We adjust the shape and duration of the waveforms on the AWG, as well as the acquisition time, skip time and bandwidth of the digitizer. Once the signal is acquired, it can be demodulated to provide the magnitude, phase, real and imaginary part of the pulse. The

skip time in the digitizer should account for the flight time of the signal through the system and the ring-up time of the cavity, given by the linewidth of its resonance κ. The digitizer will demodulate the readout pulse, whose phase ϕ contains information about the qubit state. The time delay between the pulses, which is a key magnitude to determine the coherence time of the qubit, can be modified in situ. A typical qubit drive pulse is ~ 300 nanoseconds long, while the readout pulse is usually a few microseconds long. We verified the pulse sequences (drive pulses plus readout) using a Rigol oscilloscope.

3.4. State discrimination

The key step before performing time domain measurements like Rabi oscillations [14] is state discrimination. Proper state discrimination requires determining the state of the qubit in real time with high fidelity. For that purpose, the shift of the cavity mode due to qubit excitation is no longer the best choice. It is more convenient to look at the phase ϕ acquired by the pulse after interacting with the cavity. The impedance of the qubit is state-dependent so the transmitted pulses will have a state-dependent phase. This phase can be computed from the I and Q components according to equation 5. In Figure 7a the phase of the acquired pulses after going through the cryostat is shown with qubit drive (at 4.81 GHz, red) and without it (blue). The acquired phase of the transmitted pulses is clearly different for the two qubit states.

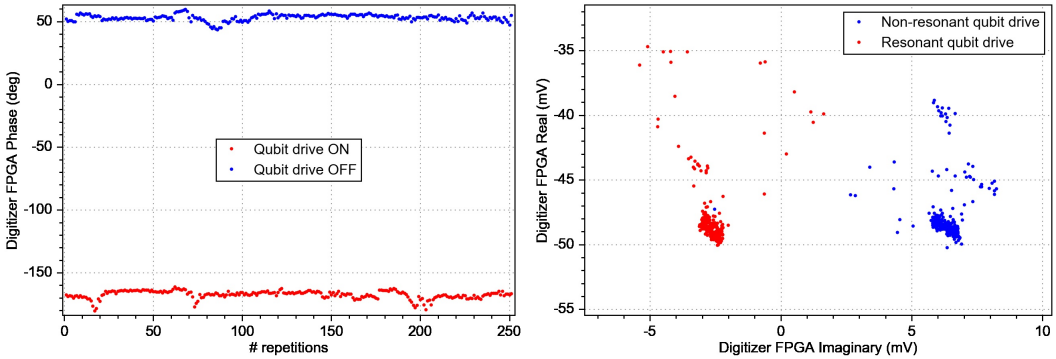

Figure 7: a) Phase of the transmitted pulses with the resonant qubit drive on (red) and off (blue). b) State discrimination on the IQ plane for resonant qubit drive (4.81 GHz, red) and non-resonant qubit drive (3GHz, blue).

The IQ components can also be plotted in phasor representation using the IQ plane. The digitizer acquires signals that rotate on this plane at an angular frequency w_{IF}. After demodulation, the trace of each transmitted pulse constitutes a point in this plane. After averaging ($10^3 - 10^4$ times) and repeating the experiment several times, each qubit state (ground or excited, for instance) will have a corresponding cluster of points on the IQ plane. These clusters can be used to determine the state of the qubit. In Figure 7b, state tomography on the IQ plane is shown for a different measurement, in which the qubit drive was set on-resonance (4.81 GHz, red) or out of resonance (3 GHz, blue). High-fidelity state discrimination had not been achieved at the time of writing this thesis, but there are some promising measurements which resemble the expected outcome of the coherent qubit readout.

The main issue restricting proper state discrimination is a triggering issue within the Keysight PXIe chassis, where the AWG and digitizer are located. This system is failing to send the proper triggers, limiting the timing precision of the signal acquisition. All pulsed measurements were perfomed using an external triggering source for AWG and digitizer (markers from an external AWG waveform). Solving this problem should enable fast and reliable state discrimination, allowing to obtain statistics from the qubit response in order characterize its properties. For instance, the next steps would comprise calibrating a Rabi pulse, inducing Rabi oscillations and performing Ramsey and spin echo measurements.

4. Conclusions

We have presented a broad review of an experimental setup for coherent control of superconducting quantum bits. All the key features of such an experiment, like the basics of transmon qubits, cryogenic methods and microwave signal processing, have been covered. We conducted spectroscopic measurements of the energy transitions of the transmon qubit, together with pulsed measurements that allowed us to obtain partial results for state discrimination. High-fidelity state discrimination will unlock the study of the coherence of the qubit, as well as the implementation of one-qubit protocols.

Acknowledgments

I would like to thank the entire QUANTIC group at BSC and IFAE, especially Pol Forn Díaz as my supervisor and David López - Núñez as my coworker in this project. Thanks to the Physics and Engineering of Nanodevices group at ICN2 for letting us use their lab space and equipment. Also thanks to all the undergraduate students that have collaborated in this project. Finally, thanks to my family for all their support during this time.

References

[1] DiVincenzo D P , Fortschritte der Physik **48**, 771-783 (2000)
[2] Keller A J *et al* , Appl. Phys. Lett. **111**, 042603 (2017)
[3] Koch J *et al* , Phys. Rev. A **76**, 04319 (2007)
[4] Rigetti C *et al* , Phys. Rev. B **86**, 100506, (2012)
[5] Naghiloo M, Lab M , arXiv 1904.09291, 2019
[6] Vool U, Devoret M , International Journal Circuit Theory and Applications **45**, 7 (897-934), (2017)
[7] Stenholm S , Journal of Physics B, **46**, 22 (2013)
[8] Schuster D I, *Circuit Quantum Electrodynamics*, PhD Thesis, (2007)
[9] Oliver W D *et al* , Appl. Phys. Rev. **6**, 021318, (2019)
[10] Jin X Y *et al* , Phys. Rev. Lett. **114**, 24 , 240501, (2015)
[11] Pobell F , *Matter and methods at low temperatures* , Springer (1996)
[12] Vepsäläinen A *et al* , Quant. Sci. Tech. **3**, 2, (2018)
[13] Paraoanu G S *et al* , Sci. Adv. **5**, 2, (2019)
[14] Wallraff A *et al* , Phys. Rev. Lett. **95**, 060501, (2005)

Appendix A

Table of experimental parameters

Bare cavity mode (w_c)	*Measured*	$2\pi \times$ 7.89 GHz
First cavity dressed mode ($w_c^{\|0\rangle}$)	*Measured*	$2\pi \times$ 7.8945 GHz
Second cavity dressed mode ($w_c^{\|1\rangle}$)	*Measured*	$2\pi \times$ 7.893 GHz
Resonator linewidth (κ)	*Measured*	$2\pi \times$ 1.86 MHz
0-1 qubit transition (w_{01})	*Measured*	$2\pi \times$ 4.81 GHz
0-2 qubit transition ($w_{02}/2$)	*Measured*	$2\pi \times$ 4.66 GHz
1-2 qubit transition (w_{12})	*Measured*	$2\pi \times$ 4.49 GHz
Resonator ring-up time (τ_r)	$\tau_r = \frac{1}{\kappa}$	0.537 μs
Loaded quality factor (Q_L)	$Q_L = \frac{w_c}{\kappa}$	4×10^3
Detuning (Δ_{01})	$\Delta_{01} = w_{01} - w_c$	$2\pi \times$ -3.08 GHz
Anharmonicity (α)	$\alpha = w_{12} - w_{01}$	$2\pi \times$ -324 MHz
Dispersive shift (χ)	$\chi = w_c^{\|0\rangle}$ - $w_c^{\|1\rangle}$	$2\pi \times$ 1.5 MHz
Coupling strength (g)	$g = \sqrt{\chi\Delta}$	$2\pi \times$ 67.9 MHz
Purcell loss rate (γ_P)	$\gamma_P = (\frac{g}{\Delta})^2\kappa$	$2\pi \times$ 0.89 kHz
Transmon charging energy ($\frac{E_C}{\hbar}$) Josephson energy ($\frac{E_J}{\hbar}$)	$\hbar w_{01} = \sqrt{8E_CE_J}$ - E_C $\hbar w_{12} = \sqrt{8E_CE_J}$ - $2E_C$	$2\pi \times$ 320 MHz $2\pi \times$ 10.28 GHz

Table 1: Experimentally determined parameters for the transmon qubit and the cavity. Note that the measured 0-2 qubit transition energy is half its actual value, as it corresponds to the absorption of two photons of frequency $w_{02}/2$.

Appendix B

Pulses and pulse sequences

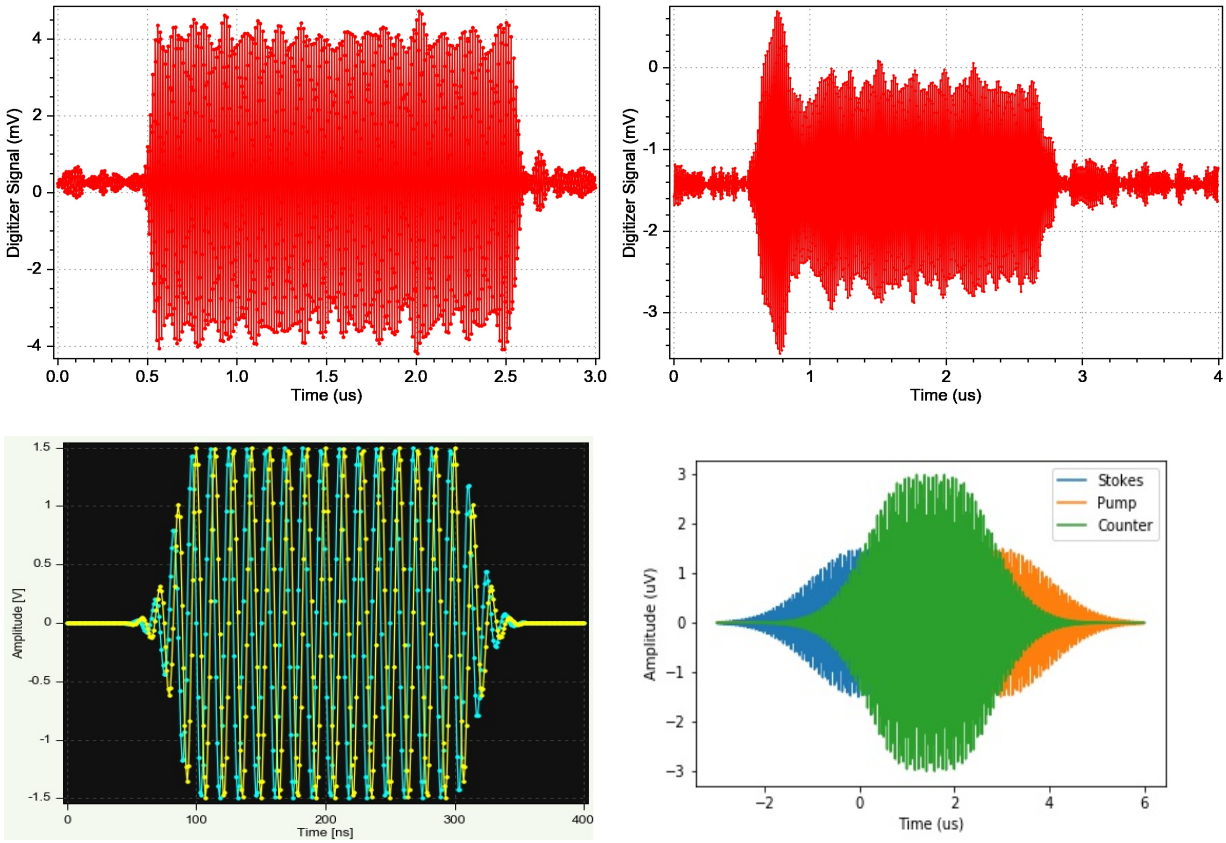

Figure 8: **Top left:** generated IQ waveform for the readout pulse. **Top right:** acquired readout pulse after resonant transmission through the cavity. **Bottom left:** short qubit drive pulse with I (yellow) and Q (blue) components. **Bottom right:** pulse sequence generated in Python for a superadiabatic STIRAP protocol [13]